

Uncertainty quantification of wall shear stress in intracranial aneurysms using a data-driven statistical model of systemic blood flow variability

Ali Sarrami-Foroushani, Toni Lassila, Ali Gooya, Arjan J. Geers, Alejandro F. Frangi



PII: S0021-9290(16)31084-3
DOI: <http://dx.doi.org/10.1016/j.jbiomech.2016.10.005>
Reference: BM7913

To appear in: *Journal of Biomechanics*
Accepted date: 9 October 2016

Cite this article as: Ali Sarrami-Foroushani, Toni Lassila, Ali Gooya, Arjan J. Geers and Alejandro F. Frangi, Uncertainty quantification of wall shear stress in intracranial aneurysms using a data-driven statistical model of systemic blood flow variability, *Journal of Biomechanics* <http://dx.doi.org/10.1016/j.jbiomech.2016.10.005>

This is a PDF file of an unedited manuscript that has been accepted for publication. As a service to our customers we are providing this early version of the manuscript. The manuscript will undergo copyediting, typesetting, and review of the resulting galley proof before it is published in its final citable form. Please note that during the production process errors may be discovered which could affect the content, and all legal disclaimers that apply to the journal pertain.

Uncertainty quantification of wall shear stress in intracranial aneurysms using a data-driven statistical model of systemic blood flow variability

Ali Sarrami-Foroushani^a, Toni Lassila^a, Ali Gooya^a, Arjan J. Geers^b,
Alejandro F. Frangi^{a,*}

^a*Centre for Computational Imaging and Simulation Technologies in Biomedicine (CISTIB),
Department of Electronic and Electrical Engineering, The University of Sheffield, Sheffield,
UK*

^b*Centre for Cardiovascular Science, University of Edinburgh, UK*

Abstract

Adverse wall shear stress (WSS) patterns are known to play a key role in the localisation, formation, and progression of intracranial aneurysms (IAs). Complex region-specific and time-varying aneurysmal WSS patterns depend both on vascular morphology as well as on variable systemic flow conditions. Computational fluid dynamics (CFD) has been proposed for characterising WSS patterns in IAs; however, CFD simulations often rely on deterministic boundary conditions that are not representative of the actual variations in blood flow. We develop a data-driven statistical model of internal carotid artery (ICA) flow, which is used to generate a virtual population of waveforms used as inlet boundary conditions in CFD simulations. This allows the statistics of the resulting aneurysmal WSS distributions to be computed. It is observed that ICA waveform variations have limited influence on the time-averaged WSS (TAWSS) on the IA surface. In contrast, in regions where the flow is locally highly multidirectional, WSS directionality and harmonic content are strongly affected by the ICA flow waveform. As a consequence, we argue that the effect of blood flow variability should be explicitly considered in CFD-based IA rupture assessment to prevent confounding the conclusions.

*Corresponding author: Alejandro F. Frangi, e-mail: a.frangi@sheffield.ac.uk,
tel: +44 114 2220153, fax: +44 114 2227890

Keywords: intracranial aneurysms, multidirectional flow, wall shear stress, computational fluid dynamics, uncertainty quantification

1 Introduction

2 Pro-inflammatory responses in the vascular endothelium play a key role in
 3 intracranial aneurysm (IA) growth and rupture (Meng et al., 2014). The driv-
 4 ing factor behind this response is hypothesised to be wall shear stress (WSS),
 5 defined as the frictional force of blood on the vessel wall. Localised adverse
 6 WSS patterns, i.e., spatiotemporal distribution of hemodynamic WSS on the
 7 aneurysm sac, have been shown by Feaver et al. (2013) to correlate with the ex-
 8 pression of transcription factors related to inflammation (such as NF- κ B), and
 9 have been shown by Davies (2009), Chiu and Chien (2011) and, Mohamied et al.
 10 (2015) to correlate with locations of atherosclerotic lesions on the vessel wall.
 11 Several attempts have been made to further characterise the atherogenic WSS
 12 patterns by looking into, e.g., WSS magnitude oscillations (Lee et al., 2009; Ku
 13 et al., 1985), temporal and spatial gradients (DePaola et al., 1992; Dolan et al.,
 14 2013), and the harmonic content of the WSS waveforms (Feaver et al., 2013;
 15 Himburg and Friedman, 2006).

16 Evaluation of WSS from phase contrast magnetic resonance imaging is not
 17 reliable enough to provide quantitative measures (Boussel et al., 2009). There-
 18 fore, computational fluid dynamics (CFD) has been proposed as a tool for char-
 19 acterising WSS patterns. WSS multidirectionality has been recently used to
 20 characterise atherogenic flows in CFD simulation studies by Mohamied et al.
 21 (2015), and Peiffer et al. (2013a). However, CFD-based studies are contro-
 22 versial among interventional neuroradiologists and have not become widely ac-
 23 cepted in clinical decision making. Such controversies can be found in e.g.
 24 Kallmes (2012), Cebal and Meng (2012), Valen-Sendstad and Steinman (2014),
 25 and Xiang et al. (2014b), where the clinicians and CFD modellers discussed
 26 the confounding nature and unreliability of various CFD-based haemodynamic
 27 variables and the importance of assumptions and uncertainties associated to

CFD models. Failure to address underlying variations in systemic blood flow due to the state of the patient (e.g., level of stress, physical activity, sleep, etc.) and its effect on WSS patterns may be one of the reasons behind this perceived unreliability.

Our primary aim is to quantify the effect of flow waveform variability on the hemodynamic WSS over the intracranial aneurysm surface. Boundary conditions in CFD models are typically either drawn from literature data or obtained by patient-specific flow imaging over a few heartbeats. Neither approach reproduces the *intra-subject variability* of systemic blood flow arising due to the presence of dynamic regulatory systems. The sensitivity of the intra-aneurysmal haemodynamics to the systemic flow conditions has been explored in various studies. For example, Geers et al. (2014) found a 20% increase in flow rate to correspond to a 27% increase in aneurysmal WSS; Xiang et al. (2014a) found different flow rate waveforms with the same time-averaged inflow rate to produce almost identical WSS distributions and WSS magnitudes, similar OSI distributions, but drastically different OSI values; and Morales and Bonnefous (2015) observed that the spatiotemporal-averaged aneurysmal WSS varies quadratically with the inflow rate. However, CFD models of vascular blood flow still mostly report deterministic flow results.

To address this problem, we construct a Gaussian process model (GPM) for generating internal carotid artery (ICA) waveforms. The GPM is calibrated against the data from Ford et al. (2005) on ICA flow measurements across a cohort of 17 young adults. The variability due to flow uncertainty is measured in three quantities of interest: time averaged WSS (TAWSS), oscillatory shear index (OSI), and transverse WSS (TransWSS), and means and confidence intervals are computed for each. In this way, we achieve a novel combination of CFD simulations and statistical models that: 1) incorporates physiological flow measurements, 2) is more systematic than previous approaches for quantifying flow uncertainty, and 3) can be fitted to the characteristics of particular cohorts.

Classifying IAs by their rupture likelihood is currently performed by looking at morphological features and patient-specific risk factors (Bederson et al.,

2000). Machine learning has been proposed to aid in this task. Xiang et al. (2011) used morphological and hemodynamic features assessed on a cohort of 119 patients to train a logistic regression model for IA classification. Bisbal et al. (2011) performed an exhaustive evaluation of seven different classifiers trained on 60 different features identified as being significant. Using the bounds on WSS uncertainty computed in this study, we explore what happens when flow uncertainties are incorporated into a classifier similar to that of Xiang et al. (2011). The results demonstrate that the effect of flow variability on IA classifiers should be explicitly considered to avoid biasing effects that may confound the conclusions of CFD studies used to predict IA rupture likelihood.

Materials and Methods

Image-based patient-specific intracranial aneurysm models

Patient-specific surface models for two saccular IAs from the @neurIST cohort were previously reconstructed from three-dimensional rotational angiography as described in by Villa-Uriol et al. (2011) using the geodesic active regions approach of Bogunović et al. (2011). Both IAs were located on the ophthalmic segment of the left internal carotid artery. During the follow-up period, the aneurysm in patient 1 ruptured, whereas the one in patient 2 did not rupture. Vascular models were discretised using unstructured volumetric meshes in ANSYS ICEM v16.2 (Ansys Inc., Canonsburg, PA, USA). Tetrahedral elements with maximum edge size of 0.2 mm were used and three layers of prismatic elements with an edge size of 0.1 mm were used to create boundary layers. The total number of elements were 2.2 and 6.6 million and mesh densities were 3025 and 3315 elements per mm^3 for patients I and II, respectively.

Computational fluid dynamics simulations

Blood flow in the IA was modelled using the incompressible unsteady Navier-Stokes equations. Blood was assumed to be a Newtonian fluid of density 1066 kg/m^3 and viscosity of 0.0035 Pa·s. Peak systolic Reynolds numbers at the

inlet ranges from 338 to 532, and no turbulence modelling was performed. To ensure fully-developed flow, the computational domain was extended at the inlet boundary by an entrance length proportional to the inlet boundary maximum Reynolds number. The Navier-Stokes equations were solved in ANSYS CFX v16.2 (Ansys Inc., Canonsburg, PA, USA) using a finite-volume method. The cardiac cycle was discretised in time into 200 equal steps. Element and time-step sizes were set according to the @neurIST processing toolchain where mesh and time-step size independency tests were performed on WSS, pressure, and flow velocity at several points in the computational domain as described by Villa-Uriol et al. (2011). Arterial distensibility was not considered in this study (rigid-wall assumption).

Inlet boundary conditions and generation of ICA waveforms

A Gaussian process model (GPM) (see e.g. Williams and Rasmussen (2006) for details) was used to generate multiple inflow waveforms that mimicked the inter-subject flow variability at the ICA. The GPM was trained on subject-specific data from the study of Ford et al. (2005) describing ICA flow measurements in 17 young adults. In that work, descriptive statistics of the reference flow rate waveform were reported in terms of mean values and variances of both time and flow rate at 14 fiducial landmarks. Flow rate mean values and variances were used to generate the GPM in this study. Any GPM is defined by its mean waveform plus a covariance function. Since the ICA flow waveform was smooth, continuous, and differentiable, the covariance function was chosen to be a squared exponential, $\sigma^2(t_j, t_k) = \sigma_0^2 \exp(-||t_j - t_k||_T^2 / 2L^2)$, with parameters σ_0 and L (Williams and Rasmussen, 2006). The distance metric was chosen as $||t_j - t_k||_T := \min\{|t_j - t_k|, |t_j - t_k + T_{\text{period}}|, |t_j - t_k - T_{\text{period}}|\}$ to get periodic waveforms, where T_{period} was the normalised cardiac cycle length and $t_j, t_k \in [0, T]$. As a stationary Gaussian process could not fully fit the observed data (variance at systolic peak was greater than during diastole), a symmetric bell-shaped function, f , was used to introduce non-stationarity in the process.

$$f(t_j, t_k) = s_d + \frac{1}{\frac{1}{s_{ps}} + \left| \frac{\max(t_j, t_k) - x_{ps}}{2} \right|^4} \quad (1)$$

In equation (1), $s_d \in [0, 1]$ and $s_{ps} \in [0, 1]$ are parameters controlling the variance during diastole and at peak systole, respectively; and, x_{ps} is the peak systolic landmark number. As reported by Ford et al. (2005), the ICA waveform systolic variance is approximately four times greater than diastolic variance and the systolic peak is the third landmark on the ICA waveform. Thus, in equation (1) the parameter s_{ps} was replaced by $4s_d$ and x_{ps} was set to 3.

Finally, the GPM mean waveform was set to the mean ICA waveform taken from Ford et al. (2005); and the GPM covariance function $\sigma^2(t_j, t_k)$ was constructed as

$$\sigma^2(t_j, t_k) = f(t_j, t_k) \cdot \sigma_0^2 \cdot \exp \left(-\min \{ |t_j - t_k|, |t_j - t_k + T_{\text{period}}|, |t_j - t_k - T_{\text{period}}| \} / 2L^2 \right). \quad (2)$$

Random realisations of the GPM was then used GPM-generated ICA waveforms. To fit the process covariance σ_0^2 and correlation length L to that observed in the measurements, for each $s_d \in [0, 1]$, a two-dimensional numerical optimisation problem was solved based on the cost function, g , that penalised values exactly equal to the mean waveform or greater than twice the standard deviation for each landmark.

$$g(y_j) = \begin{cases} P_o(y_j - (\bar{y}_j + 2SD_j)) & \bar{y}_j + 2SD_j \leq y_j \\ \frac{-P_m}{2SD_j}|y_j - \bar{y}_j| + P_m & \bar{y}_j - 2SD_j \leq y_j \leq \bar{y}_j + 2SD_j \\ P_o(y_j - (\bar{y}_j - 2SD_j)) & y_j \leq \bar{y}_j - 2SD_j \end{cases} \quad (3)$$

For each landmark j , y_j is the value of ICA flow generated by the GPM; and, \bar{y}_j and SD_j are the mean and standard deviation reported by Ford et al. (2005). Penalty parameters P_m and P_o penalise y_i values that are exactly equal to the mean or are deviated more than twice the standard deviation from the mean.

136 A virtual population of 50 internal carotid flow waveforms was then gener-
 137 ated and used as inlet boundary conditions to the CFD models. To maintain
 138 a physiological arterial WSS of 1.5 Pa and to enable population-wide compar-
 139 isons, Poiseuille's law was used to scale the GPM-generated waveforms such
 140 that the time-averaged WSS was 1.5 Pa at the inlet. Fig. 1(a) shows the 95%
 141 confidence bounds of flow at the fiducial landmarks (black bars), and a virtual
 142 population of internal carotid artery flow waveforms generated from the Gaus-
 143 sian process model (red curves). More details about GP modelling of the ICA
 144 flow waveforms are presented in the Supplementary Material.

145 *Outlet boundary conditions*

146 A two-element windkessel (RC) boundary condition model was assigned at
 147 the outlet boundaries. The RC windkessel model acts as a low-pass filter with
 148 a RC time constant $\tau = R \times C$. To guarantee that the terminal RC circuit
 149 converges to the ultimate pulsatile pressure and the solution is independent
 150 from the initial transient numerical effects, each simulation was run for certain
 151 number of cycles, defined as $nCycle = \left\lceil \frac{\tau}{T_{period}} \right\rceil + 1$, where $\lceil x \rceil$ symbolized the
 152 ceil function. Results from the last cardiac cycle were then used to calculate
 153 the hemodynamic parameters of interest. The resistance and capacitance values
 154 of the windkessel model were chosen to maintain a physiological range of ICA
 155 pressure and pulsatility for each particular patient. To enable rapid parameter
 156 tuning, a surrogate model was built using polynomial response surfaces to ap-
 157 proximate the mean arterial pressure (MAP) and pressure wave pulsatility index
 158 (PPI) of the flow for each (R,C) pair. A Chebyshev grid of 81 (9×9) points was
 159 created on a 2D physiological range of variability for R and C (reported in e.g.
 160 Brown et al. (2012); Reymond et al. (2011, 2009); Stergiopulos et al. (1992);
 161 Vignon-Clementel et al. (2010)) in such a way that each point on the grid was
 162 associated with a pair of R and C values. A total of 81 CFD simulations were
 163 performed while recording the observed values of steady-state mean arterial
 164 pressure (MAP) and pressure wave pulsatility index (PPI) in the ICA for each
 165 simulation after $nCycle$ heartbeat cycles. To develop a surrogate model of ICA

MAP and PPI vs terminal resistance and capacitance, MAP and PPI surfaces were linearly interpolated over a uniform grid of 100×100 . The surrogate model was used to select values R and C values in such a way that when the reference inflow waveform were applied at the inlet boundary, the model provides ICA pressures with MAP and PPI matching clinically measured values of 90 mmHg and 0.5 from the normal individual, respectively. Fig. 1(b) and Fig. 1(c). show the response surfaces of MAP and PPI against terminal resistance and capacitance for patient 1. Fig. 1(d), values of R and C at the point, where MAP = 90 mmHg and PPI = 0.5 intersects, were selected as optimized windkessel parameters for patient 1. As mentioned above, a derivation of the Poiseuille's law that relates the inflow rate to the WSS and vessel's inlet cross-sectional area was used to scale the time-averaged flow rate in the parent vessel for each patient. Since the time-averaged flow rates are different in patient 2, the resistance and capacitance values from the first patient's surrogate model need to be scaled using factor α defined as $\alpha = \text{inflow}_{tav,1} / \text{inflow}_{tav,2}$, where $\text{inflow}_{tav,1}$ and $\text{inflow}_{tav,2}$ are time-averaged inflow rates for patients 1 and 2. The terminal resistance and capacitance were then scaled as $R_2 = (1/\alpha) \times R_1$ and $C_2 = \alpha \times C_1$, respectively.

Fig. 1(e) shows reference inflow waves for patients 1 and 2. Fig. 1(f) shows that, applying the windkessel outlet boundary condition with tuned R and C values, the same desired ICA pressure has been obtained for patients 1 and 2 with different inflow waveforms. Since the time-averaged inflow rate was kept constant and only waveform shapes varied across the virtual population, the same R and C values as those tuned with the reference inflow waveforms were used for all 50 CFD simulations on each patient.

Data analysis

Wall shear stress (WSS), $\tau_w(x, t)$, is a time-varying vector field that represents the tangential component of the traction vector on the wall. We assessed the magnitude, pulsatility, directionality and the harmonic content of the WSS waveforms on the aneurysm wall using several derived quantities of interest.

196 *WSS magnitude*

197 Time-averaged WSS (TAWSS) was calculated by averaging the magnitude
198 of WSS vector at each surface node over the cardiac cycle.

$$\text{TAWSS}(x) = \frac{1}{T_{\text{period}}} \int_{T_0}^{T_0+T_{\text{period}}} |\boldsymbol{\tau}_w(x, t)| dt \quad (4)$$

199 The variables T_0 and $T_0 + T_{\text{period}}$ are the starting point (3rd heartbeat) and
200 the length of the cardiac cycle over which the WSS was integrated, respectively.

201 *WSS directionality*

As suggested by Mohamied et al. (2015) and Peiffer et al. (2013a,b), to assess the directionality of WSS we used both OSI and TransWSS. The oscillatory shear index was calculated as

$$\text{OSI} = \frac{1}{2} \left(1 - \frac{|\int_{T_0}^{T_0+T_{\text{period}}} \boldsymbol{\tau}_w(x, t) dt|}{\int_0^{T_{\text{period}}} |\boldsymbol{\tau}_w(x, t)| dt} \right) \quad (5)$$

and transverse WSS was calculated as defined by Peiffer et al. (2013a)

$$\text{transWSS} = \frac{1}{T_{\text{period}}} \int_{T_0}^{T_0+T_{\text{period}}} |\boldsymbol{\tau}_w(x, t) \cdot \hat{q}| dt, \quad (6)$$

where $\hat{q} = \hat{p} \times \hat{n}$ and the unit vector \hat{p} is the direction of the time-averaged WSS vector, \hat{n} is the surface normal, and consequently the unit vector \hat{q} is located in the same plane as \hat{p} and its direction is perpendicular to the time-averaged WSS vector. The unit vector \hat{p} was calculated as

$$\hat{p} = \frac{\int_{T_0}^{T_0+T_{\text{period}}} \boldsymbol{\tau}_w(x, t) dt}{|\int_{T_0}^{T_0+T_{\text{period}}} \boldsymbol{\tau}_w(x, t) dt|} \quad (7)$$

202 As long as a preferred time-averaged direction of flow exists, TransWSS ranges
203 from 0 to TAWSS. As the TAWSS takes substantially different values at aneurys-
204 mal regions with disturbed or regular flow, we defined the relative transWSS
205 (rTransWSS) as the TransWSS normalised TransWSS by the TAWSS at each
206 surface point.

WSS harmonics

As indicated by Lee et al. (2009), despite the multidirectional nature of blood flow in patient-specific vascular models, most experimental studies are performed under uniaxial flow due to constraints in experimental flow setups. Recently, WSS projections onto a reference axial direction were performed to rectify multidirectional flows and make them comparable to the flows used for *in vitro* experiments of Arzani and Shadden (2016) and Morbiducci et al. (2015). However, since rectifying the WSS signal combines the magnitude and directionality aspects of the WSS vector and influences its harmonic content, we chose to perform a harmonic analysis on both the original and the rectified WSS signals. It has been observed that most physiological waveforms can be accurately reconstructed by the first ten or fewer harmonics (Nichols et al., 2011). Studying the first eight harmonics of the WSS signals at the ICA, Feaver et al. (2013) showed that the endothelial inflammatory responses are mainly regulated by the first harmonic of the WSS signal. Thus, in this study, we based our harmonic analyses on the first eight harmonics of the WSS signals. We calculated the axial WSS as the component of time-varying WSS vector projected onto the unit vector \hat{p} . The fast Fourier transform was used to describe the time-varying aneurysmal WSS and axial WSS waveforms in the frequency domain and extract the amplitudes of the harmonics zeroth to eighth. It has been hypothesised that dominance of frequencies higher than the heart rate in the WSS magnitude signal triggers inflammatory responses in the vascular endothelium (Himburg et al., 2007; Feaver et al., 2013). The dominant harmonic (DH) is another quantity of interest defined as the harmonic with the greatest amplitude by Himburg and Friedman (2006). As shown by Lee et al. (2009), DH is independent from other WSS-related variables. In this study we also used DH to investigate how waveform variability in the parent vessel affect the dominant frequency of the time-varying WSS magnitude over the aneurysm sac.

235 *Intracranial aneurysm rupture prediction*

236 To evaluate the effect of WSS uncertainty in IA rupture prediction, a differ-
 237 ent subset of 38 IAs all located at the sylvian bifurcation of the middle cerebral
 238 artery (MbifA-type) were selected from the @neurIST cohort and processed
 239 through the CFD pipeline as described in the Methods section. For this co-
 240 hort, outlet branches were automatically clipped 20 mm after their proximal
 241 bifurcation. Branches shorter than 20 mm were extruded before truncation.
 242 Zero-pressure boundary conditions were then imposed at all outlets. As a full
 243 CFD simulation of all 50×38 cases would have been prohibitively costly, three
 244 representative waveforms were instead used for each of the 38 cases: mean flow,
 245 minimum flow and maximum flow predicted by the GPM model. TAWSS, OSI,
 246 and TransWSS were post-processed for each of these simulations and spatially
 247 averaged over the aneurysm sac to arrive at the feature values used for classifi-
 248 cation. These three different flow waveforms were then used to train a logistic
 249 regression model classifier similar to that of Xiang et al. (2011):

$$\text{logit}(P_r) = \beta_0 + \beta_1 \text{OSI} + \beta_2 \text{TAWSS},$$

250 where P_r is the model-predicted probability that the aneurysm was of the
 251 ruptured type, and the logit function is defined as $\text{logit}(p) = \log\left(\frac{p}{1-p}\right)$. The
 252 regression coefficients $\beta_0, \beta_1, \beta_2$ were obtained through standard generalised
 253 regression techniques, and were used to define the corresponding odds ratios
 254 ($\text{OR}_{\text{OSI}} = \exp(\beta_1)$ etc.), signifying how the odds of rupture increase by each
 255 unit increase in OSI.

256 **Results**

257 Fig. 2 shows the mean values and the coefficients of variation (CoV) for
 258 TAWSS, OSI, and rTransWSS on the aneurysm sac simulated by CFD over the
 259 population of 50 difference ICA waveforms. In both cases, the ICA waveform
 260 variability had limited effects ($\text{CoV} < 0.05$) on the TAWSS. However, the ef-
 261 fects were remarkable on WSS directional variability. CoVs for aneurysmal OSI

262 and rTransWSS were both greater than 0.4 at regions where the WSS vectors
 263 had low magnitude but were directionally varying in time (disturbed flow re-
 264 gions). Waveform variability in the parent vessel had less significant effects on
 265 the WSS directionality at regions where shear stresses are higher and remain
 266 mostly unidirectional throughout the cardiac cycle (stable flow regions).

267 Fig. 3 shows mean values and CoVs for the dominant harmonic (DH) over
 268 the aneurysm sac. On both aneurysms, there are regions where the dominant
 269 frequencies are up to 5 times greater than the fundamental frequency (the heart
 270 rate). Results show that ICA waveform variability highly influences the time-
 271 varying WSS signal at regions where the higher harmonics dominate ($\text{CoV} >$
 272 2). Similar to the directionality, less significant effects were observed at regions
 273 with regular pulsatile flow dominated by the heart rate frequency (regions where
 274 DH is unity).

275 However, DH was originally defined for a unidirectional axial flow and may
 276 not lead to clinically interpretable results in multidirectional nonaxial flows (Lee
 277 et al. (2009); Morbiducci et al. (2015)). To alleviate this issue in the complex
 278 aneurysmal flows, we followed the method presented by Lee et al. (2009) and
 279 rectified WSS vectors by projecting them on the time-averaged WSS direction as
 280 a reference axial direction. Fig. 3 also shows the effect of parent vessel waveform
 281 variability on the harmonic content of the axial WSS magnitude signal. Results
 282 show that rectification of the WSS signal increased the DH at regions where flow
 283 is multidirectional. This can be attributed to the previously mentioned effects
 284 of ICA waveform variations on the WSS directionality, which implicitly affected
 285 the WSS magnitude signal during the rectification process. It can be seen that
 286 ICA waveform variability significantly influences the harmonic content of the
 287 axial WSS at disturbed flow regions ($\text{CoV} > 2$). To provide more intuition
 288 into the effects of parent vessel flow waveform variability, we illustrated the
 289 results for five manually selected representative points on the aneurysm sacs
 290 (see Supplementary Material).

	Ruptured ($N = 14$)	Unruptured ($N = 24$)	p -value
TAWSS [Pa]	3.32 (3.36)	3.76 (3.25)	0.7
OSI	12.4×10^{-3} (7.25×10^{-3})	7.79×10^{-3} (6.05×10^{-3})	0.032*
rTransWSS	0.104 (0.037)	0.088 (0.029)	0.12

Table 1: WSS quantities derived from CFD-simulations in the ruptured vs. unruptured groups of the @neurIST cohort. Values are group-wise means and standard deviations of the mean flow case. Statistical significance in univariate analysis computed using a two-sided t -test.

Effect of flow uncertainty on rupture pattern

The three WSS-derived quantities were evaluated through CFD simulations in $N = 38$ cases taken from the @neurIST database. Summary statistics of the WSS values evaluated are shown in Table 1 for the case of mean flow. An unpaired two-sided two-sample t -test was used to select the WSS-related features that were significantly different in the ruptured vs. unruptured populations. Spatially averaged OSI was significant or almost significant for all three flow cases ($p \in [0.032, 0.058]$), whereas TAWSS and TransWSS were not significant for any of the three flow cases considered ($p = 0.7$ for TAWSS and $p \in [0.12, 0.15]$ for TransWSS). This was in agreement with the analysis of Bisbal et al. (2011) (who used a superset of our data), but contradicted the observations of Xiang et al. (2014a) who obtained significance also for TAWSS. We therefore opted to train the classifier only on one feature, the OSI, leading to the regression model $\text{logit}(P_r) = \beta_0 + \beta_1 \text{OSI}$ for the rupture classification variable P_r . Before training the classifier, the OSI values were scaled so that the maximum value across the 38 cases was equal to 10. The data were divided into 19 training cases, which were used to estimate the regression coefficients, and 19 test cases, which were used for cross-validation.

The logistic regression based classifier achieved an area under the ROC curve that ranged in $\text{AUC} \in [0.8947, 0.9044]$. For the cutoff value $P_r = 0.9$, the resulting classifier achieved a sensitivity ranging in $\text{SENS} \in [79.0\%, 84.2\%]$, and a specificity ranging in $\text{SPEC} \in [79.0\%, 89.5\%]$ in the cross-validation exercise. The regression coefficients identified in each three flow cases were in the range

$\beta_0 \in [-3.59, -2.93]$ and $\beta_1 \in [0.804, 0.883]$. The corresponding odds ratio for
 OSI was in the range $OR_{OSI} \in [2.23, 2.42]$, reproducing the known correlation
 between elevated OSI and rupture status. While the accuracy of the classifier
 was only moderately affected by the flow case considered, the final rupture/no-
 rupture prediction changed as a function of flow for 4 cases out of 19.

Discussion

Recent evidence links the region-specific inflammatory phenotype of the en-
 dothelial cells to both directionality and harmonic content of the time-varying
 WSS vector field (Wang et al., 2013; Peiffer et al., 2013a; Mohamied et al.,
 2015; Himburg et al., 2007; Feaver et al., 2013). Spatiotemporal variations of
 vascular WSS are driven by variabilities in the blood flow waveform and the vas-
 cular morphology. Although attempts at measuring the effect of parent vessel
 flow waveforms on WSS-related quantities of interest measuring directionality
 and harmonic content have been made by Peiffer et al. (2013a); Himburg et al.
 (2007); Feaver et al. (2013); Lee et al. (2009) and others, there are few studies
 that have systematically evaluated the sensitivity of WSS to flow variability.

Time-averaged inflow rates have been shown to affect the magnitude of
 aneurysmal WSS (Geers et al., 2014). Using one-shot measurements of patient-
 specific inflow boundary conditions has been shown to highly influence the mag-
 nitude of aneurysmal WSS when compared to results obtained from simulations
 with typical inflow boundary conditions derived from literature (Karmonik et al.,
 2010; Marzo et al., 2011; McGah et al., 2014). However, *in vivo* flow measure-
 ments typically record systemic flow only for a few cardiac cycles, and therefore
 do not represent the full range of flow variability. In the recent study of Xiang
 et al. (2014a), the effect of four different inlet waveforms on the space-averaged
 OSI was tested using CFD. Different waveforms produced drastically different
 absolute values of OSI, but similar OSI distributions over the aneurysm sac. A
 linear relationship was also observed between the spatially averaged OSI values
 calculated using different inflow waveforms, which suggests that changing the

343 waveform did not consistently change the rupture risk ranking of aneurysms.
 344 Absolute values of OSI might, however, not be a robust criteria for clinical deci-
 345 sion making unless the flow-related uncertainty is explicitly taken into account.

346 We evaluated flow-induced WSS variability by performing simulations us-
 347 ing boundary conditions sampled from a statistical description of inter-subject
 348 flow variability. When keeping the time-averaged flow rate fixed, variations in
 349 ICA flow waveforms had limited effects on the TAWSS over the aneurysm sac.
 350 However, it was found that WSS directionality measures (OSI and rTransWSS)
 351 in the disturbed flow regions (atheroprone regions) were very sensitive to flow
 352 waveform variability, although the effects were limited in regular flow regions
 353 where a preferred direction of flow exists (atheroprotective regions). To shed
 354 more light on regional effects of flow waveforms on the aneurysmal WSS, we
 355 defined atheroprone regions as regions where WSS is low ($\text{TAWSS} < 1 \text{ Pa}$)
 356 and multidirectional ($\text{rTransWSS} > 0.3$) and atheroprotective regions as re-
 357 gions where $\text{TAWSS} > 3 \text{ Pa}$ and almost unidirectional ($\text{rTransWSS} < 0.1$).
 358 These thresholds were conservatively chosen according to studies where WSS
 359 magnitude and directionality were correlated with pro-inflammatory endothe-
 360 lial phenotypes (Wang et al., 2013; Peiffer et al., 2013a; Mohamied et al., 2015;
 361 Feaver et al., 2013). As shown in Fig. 4 for the two IAs considered, varying
 362 inflow waveform had limited effects on the TAWSS in both disturbed flow and
 363 regular flow regions ($\text{CoV} < 0.1$). However, WSS directionality in disturbed
 364 flow regions is strongly affected by the inflow waveform (CoV up to 2 with a
 365 median at 0.25), when compared to the protective regions. This implies the im-
 366 portance of flow waveform uncertainty in aneurysmal regions which are prone
 367 to inflammatory phenotypes and potential rupture. Mohamied et al. (2015)
 368 observed that despite OSI, TransWSS correlated significantly with atheroscle-
 369 rotic lesions in rabbits' aorta. Comparing OSI and rTransWSS as measures of
 370 WSS directionality, we observed that these two variables are in stronger cor-
 371 relation at regular flow (atheroprotective) regions (Pearson $r = 0.94$ and 0.96
 372 for aneurysms 1 and 2, respectively; $p < 10^{-5}$) when compared to disturbed
 373 flow (atheroprone) regions where flow is highly multidirectional (Pearson $r =$

0.75 and 0.66 for aneurysms 1 and 2, respectively; $p < 10^{-5}$). A point-wise comparison of OSI and rTransWSS is presented in the Supplementary Material.

We have studied variability of the DH of the local WSS signal and observed that, due to nonlinear effects due of the vascular morphology, there are regions where the dominant harmonic of the time-varying WSS signal is not the systemic fundamental frequency (heart rate). We observed that, when considering the DH of the axial WSS signals, regions with higher DH than the heart rate co-localise with the regions where flow is multidirectional. This co-localisation could be explained by the fact that axial WSS is the projection of the instantaneous WSS vector in the time-averaged WSS vector direction. Xiang et al. (2014a) observed a strong correlation between the space-averaged aneurysmal OSI and the inflow waveform pulsatility index (PI), and suggested that OSI might be mainly determined by the PI of the inlet waveform. As a subsidiary study, we investigated any possible correlation between the inflow PI and the local OSI at five points on the aneurysm sacs. At each point on the aneurysm sac, PI was calculated as the difference between maximum and minimum flow rate divided by the time-averaged flow rate during each cardiac cycle. No clear correlation was observed between inflow PI and OSI at points where the dominant frequency was higher than the heart rate (see Table 1 in the Supplementary Material). This implies that parent vessel PI (easy to measure) is not a good surrogate for evaluating aneurysmal OSI (difficult to measure).

We have also explored the effects that WSS uncertainty may have on IA rupture likelihood by using a logistic regression. In our dataset the TAWSS did not reach statistical significance in separating ruptured cases from non-ruptured cases, so that a classifier was built solely based on OSI values. Our classifier reached similar accuracy to that previously reported (sensitivity ranging in $\text{SENS} \in [79.0\%, 84.2\%]$ and specificity ranging in $\text{SPEC} \in [79.0\%, 89.5\%]$), but provided a range of values depending on the choice of input flow waveform used. While the accuracy of the classifier was similar across waveforms, the classification between likely to rupture/likely to not rupture changed in 4 out of the 19 cases when the flow solution was varied. It is our view that, due to such ef-

fects, flow-related uncertainty should be explicitly accounted for in WSS-based rupture predictions to improve their credibility.

The limitations of our study were that the blood flow was assumed to be Newtonian and arterial distensibility was not taken into account, which overestimates WSS by up to 15% Section (Steinman, 2012). Transition from laminar to turbulent flow occurs at $Re = 300-500$ in intracranial aneurysms (Yagi et al., 2013), and using laminar flow models may not capture all intra-aneurysmal flow characteristics accurately. Parabolic velocity profiles were imposed at the inlet boundaries which may lead to different flow characteristics compared to the Womersley profiles. Intra-aneurysmal hemodynamics has been shown to be sensitive to the choice of inlet location for truncating the ICA from the surrounding vascular bed (Pereira et al., 2013). To reduce such errors and allow realistic flow inside the aneurysms, all the inlets were truncated at consistent locations below the cavernous segment to include the largest possible arterial segment upstream the aneurysm (Valen-Sendstad et al., 2015). Vascular models were extruded at inlet boundaries by an entry length proportional to the specific Re to allow for fully developed flow. The flow variability model considered also modelled inter-subject variability only (rather than intra-subject), and was based on data from young adults only.

Conflict of interest statement

All the authors declare no conflicts of interest exist.

Acknowledgements

This project was partly supported by the Marie Curie Individual Fellowship (625745, A. Gooya). The aneurysm dataset has been provided by the European integrated project @neurIST (IST-027703).

References

- Arzani, A., Shadden, S.C., 2016. Characterizations and correlations of wall shear stress in aneurysmal flow. *Journal of Biomechanical Engineering* 138(1), 014503.
- Bederson, J.B., Awad, I.A., Wiebers, D.O., Piepgras, D., Haley, E.C., Brott, T., Hademenos, G., Chyatte, D., Rosenwasser, R., Caroselli, C., 2000. Recommendations for the management of patients with unruptured intracranial aneurysms a statement for healthcare professionals from the Stroke Council of the American Heart Association. *Circulation* 102(18), 2300–2308.
- Bisbal, J., Engelbrecht, G., Villa-Uriol, M.C., Frangi, A.F., 2011. Prediction of cerebral aneurysm rupture using hemodynamic, morphologic and clinical features: a data mining approach, in: A. Hameurlain, S.W. Liddle, K.-D. Schewe, X. Zhou (Eds.), *Database and Expert Systems Applications, Proc. 22nd Int. Conf. DEXA 2011, Toulouse, France, August 29–September 2, Springer LNCS* 6861. pp. 59–73.
- Bogunović, H., Pozo, J.M., Villa-Uriol, M.C., Majoie, C.B., van den Berg, R., van Andel, H.A.G., Macho, J.M., Blasco, J., San Román, L., Frangi, A.F., 2011. Automated segmentation of cerebral vasculature with aneurysms in 3DRA and TOF-MRA using geodesic active regions: an evaluation study. *Medical Physics* 38(1), 210–222.
- Boussel, L., Rayz, V., Martin, A., Acevedo-Bolton, G., Lawton, M.T., Higashida, R., Smith, W.S., Young, W.L., Saloner, D., 2009. Phase-contrast magnetic resonance imaging measurements in intracranial aneurysms in vivo of flow patterns, velocity fields, and wall shear stress: comparison with computational fluid dynamics. *Magnetic Resonance in Medicine* 61(2), 409–417.
- Brown, A.G., Shi, Y., Marzo, A., Staicu, C., Valverde, I., Beerbaum, P., Lawford, P.V., Hose, D.R., 2012. Accuracy vs. computational time: translating aortic simulations to the clinic. *Journal of Biomechanics* 45(3), 516–523.

- 458 Cebal, J.R., Meng, H., 2012. Counterpoint: realizing the clinical utility of
459 computational fluid dynamics—closing the gap. *American Journal of Neuro-*
460 *radiology* 33, 396–398.
- 461 Chiu, J.J., Chien, S., 2011. Effects of disturbed flow on vascular endothe-
462 lium: pathophysiological basis and clinical perspectives. *Physiological Re-*
463 *views* 91(1), 327–387.
- 464 Davies, P.F., 2009. Hemodynamic shear stress and the endothelium in cardio-
465 vascular pathophysiology. *Nature Reviews Cardiology* 6(1), 16–26.
- 466 DePaola, N., Gimbrone, M., Davies, P.F., Dewey, C., 1992. Vascular endothe-
467 lium responds to fluid shear stress gradients. *Arteriosclerosis, Thrombosis,*
468 *and Vascular Biology* 12(11), 1254–1257.
- 469 Dolan, J.M., Kolega, J., Meng, H., 2013. High wall shear stress and spatial
470 gradients in vascular pathology: a review. *Annals of Biomedical Engineering*
471 41(7), 1411–1427.
- 472 Feaver, R.E., Gelfand, B.D., Blackman, B.R., 2013. Human haemodynamic
473 frequency harmonics regulate the inflammatory phenotype of vascular en-
474 dothelial cells. *Nature Communications* 4. Article number: 1525.
- 475 Ford, M.D., Alperin, N., Lee, S.H., Holdsworth, D.W., Steinman, D.A., 2005.
476 Characterization of volumetric flow rate waveforms in the normal internal
477 carotid and vertebral arteries. *Physiological Measurements* 26(4), 477.
- 478 Geers, A., Larrabide, I., Morales, H., Frangi, A., 2014. Approximating hemo-
479 dynamics of cerebral aneurysms with steady flow simulations. *Journal of*
480 *Biomechanics* 47(1), 178–185.
- 481 Himburg, H.A., Dowd, S.E., Friedman, M.H., 2007. Frequency-dependent re-
482 sponse of the vascular endothelium to pulsatile shear stress. *American Journal*
483 *of Physiology - Heart and Circulatory Physiology* 293(1), H645–H653.

- 484 Himburg, H.A., Friedman, M.H., 2006. Correspondence of low mean shear and
485 high harmonic content in the porcine iliac arteries. *Journal of Biomechanical*
486 *Engineering* 128(6), 852–856.
- 487 Kallmes, D.F., 2012. Point: CFD—computational fluid dynamics or confound-
488 ing factor dissemination. *American Journal of Neuroradiology* 33, 395–396.
- 489 Karmonik, C., Yen, C., Diaz, O., Klucznik, R., Grossman, R.G., Benndorf,
490 G., 2010. Temporal variations of wall shear stress parameters in intracranial
491 aneurysms—importance of patient-specific inflow waveforms for CFD calcu-
492 lations. *Acta Neurochirurgica* 152, 1391–1398.
- 493 Ku, D.N., Giddens, D.P., Zarins, C.K., Glagov, S., 1985. Pulsatile flow and
494 atherosclerosis in the human carotid bifurcation. positive correlation between
495 plaque location and low oscillating shear stress. *Arteriosclerosis, Thrombosis,*
496 *and Vascular Biology* 5(3), 293–302.
- 497 Lee, S.W., Antiga, L., Steinman, D.A., 2009. Correlations among indicators of
498 disturbed flow at the normal carotid bifurcation. *Journal of Biomechanical*
499 *Engineering* 131(6), 061013.
- 500 Marzo, A., Singh, P., Larrabide, I., Radaelli, A., Coley, S., Gwilliam, M., Wilkin-
501 son, I.D., Lawford, P., Reymond, P., Patel, U., et al., 2011. Computational
502 hemodynamics in cerebral aneurysms: the effects of modeled versus measured
503 boundary conditions. *Annals of Biomedical Engineering* 39, 884–896.
- 504 McGah, P.M., Levitt, M.R., Barbour, M.C., Morton, R.P., Nerva, J.D., Mourad,
505 P.D., Ghodke, B.V., Hallam, D.K., Sekhar, L.N., Kim, L.J., et al., 2014.
506 Accuracy of computational cerebral aneurysm hemodynamics using patient-
507 specific endovascular measurements. *Annals of Biomedical Engineering* 42,
508 503–514.
- 509 Meng, H., Tutino, V., Xiang, J., Siddiqui, A., 2014. High WSS or low WSS?
510 complex interactions of hemodynamics with intracranial aneurysm initiation,

- 511 growth, and rupture: toward a unifying hypothesis. *American Journal of*
512 *Neuroradiology* 35(7), 1254–1262.
- 513 Mohamied, Y., Rowland, E.M., Bailey, E.L., Sherwin, S.J., Schwartz, M.A.,
514 Weinberg, P.D., 2015. Change of direction in the biomechanics of atheroscle-
515 rosis. *Annals of Biomedical Engineering* 43(1), 16–25.
- 516 Morales, H.G., Bonnefous, O., 2015. Unraveling the relationship between arte-
517 rial flow and intra-aneurysmal hemodynamics. *Journal of Biomechanics* 48(4),
518 585–591.
- 519 Morbiducci, U., Gallo, D., Cristofanelli, S., Ponzini, R., Deriu, M.A., Rizzo, G.,
520 Steinman, D.A., 2015. A rational approach to defining principal axes of mul-
521 tidirectional wall shear stress in realistic vascular geometries, with application
522 to the study of the influence of helical flow on wall shear stress directionality
523 in aorta. *Journal of Biomechanics* 48(6), 899–906.
- 524 Nichols, W., O'Rourke, M., Vlachopoulos, C., 2011. McDonald's blood flow in
525 arteries: theoretical, experimental and clinical principles. CRC Press.
- 526 Peiffer, V., Sherwin, S.J., Weinberg, P.D., 2013a. Computation in the rabbit
527 aorta of a new metric—the transverse wall shear stress—to quantify the multi-
528 directional character of disturbed blood flow. *Journal of Biomechanics* 46(15),
529 2651–2658.
- 530 Peiffer, V., Sherwin, S.J., Weinberg, P.D., 2013b. Does low and oscillatory
531 wall shear stress correlate spatially with early atherosclerosis? a systematic
532 review. *Cardiovasc. Res.* DOI: <http://dx.doi.org/10.1093/cvr/cvt044>.
- 533 Pereira, V., Brina, O., Gonzales, A.M., Narata, A., Bijlenga, P., Schaller, K.,
534 Lovblad, K., Ouared, R., 2013. Evaluation of the influence of inlet boundary
535 conditions on computational fluid dynamics for intracranial aneurysms: a
536 virtual experiment. *Journal of biomechanics* 46, 1531–1539.
- 537 Reymond, P., Bohraus, Y., Perren, F., Lazeyras, F., Stergiopulos, N., 2011.
538 Validation of a patient-specific one-dimensional model of the systemic arte-

- 539 rial tree. American Journal of Physiology-Heart and Circulatory Physiology
540 301(3), H1173–H1182.
- 541 Reymond, P., Merenda, F., Perren, F., Rüfenacht, D., Stergiopulos, N., 2009.
542 Validation of a one-dimensional model of the systemic arterial tree. American
543 Journal of Physiology - Heart and Circulatory Physiology 297(1), H208–H222.
- 544 Steinman, D.A., 2012. Assumptions in modelling of large artery hemodynamics,
545 in: D. Ambrosi, A. Quarteroni, G. Rozza (Eds.), Modeling of Physiological
546 Flows. Springer-Verlag Italia, pp. 1–18.
- 547 Stergiopulos, N., Young, D., Rogge, T., 1992. Computer simulation of arterial
548 flow with applications to arterial and aortic stenoses. Journal of Biomechanics
549 25(12), 1477–1488.
- 550 Valen-Sendstad, K., Piccinelli, M., KrishnankuttyRema, R., Steinman, D.A.,
551 2015. Estimation of inlet flow rates for image-based aneurysm cfd models:
552 where and how to begin? Annals of biomedical engineering 43, 1422–1431.
- 553 Valen-Sendstad, K., Steinman, D., 2014. Mind the gap: impact of computational
554 fluid dynamics solution strategy on prediction of intracranial aneurysm hemo-
555 dynamics and rupture status indicators. American Journal of Neuroradiology
556 35(5), 536–543.
- 557 Vignon-Clementel, I.E., Figueroa, C., Jansen, K., Taylor, C., 2010. Outflow
558 boundary conditions for 3d simulations of non-periodic blood flow and pres-
559 sure fields in deformable arteries. Comput. Methods Biomech. Biomed. Engin.
560 13(5), 625–640.
- 561 Villa-Uriol, M., Berti, G., Hose, D., Marzo, A., Chiarini, A., Penrose, J., Pozo,
562 J., Schmidt, J., Singh, P., Lycett, R., et al., 2011. @neurIST complex in-
563 formation processing toolchain for the integrated management of cerebral
564 aneurysms. Interface Focus DOI: 10.1098/rsfs.2010.0033.

- 565 Wang, C., Baker, B.M., Chen, C.S., Schwartz, M.A., 2013. Endothelial cell
566 sensing of flow direction. *Arteriosclerosis, Thrombosis, and Vascular Biology*
567 33(9), 2130–2136.
- 568 Williams, C.K., Rasmussen, C.E., 2006. Gaussian processes for machine learn-
569 ing. MIT Press 2(3).
- 570 Xiang, J., Natarajan, S.K., Tremmel, M., Ma, D., Mocco, J., Hopkins, L.N.,
571 Siddiqui, A.H., Levy, E.I., Meng, H., 2011. Hemodynamic–morphologic dis-
572 criminants for intracranial aneurysm rupture. *Stroke* 42(1), 144–152.
- 573 Xiang, J., Siddiqui, A., Meng, H., 2014a. The effect of inlet waveforms on com-
574 putational hemodynamics of patient-specific intracranial aneurysms. *Journal*
575 *of Biomechanics* 47(16), 3882–3890.
- 576 Xiang, J., Tutino, V., Snyder, K., Meng, H., 2014b. CFD: computational fluid
577 dynamics or confounding factor dissemination? The role of hemodynamics in
578 intracranial aneurysm rupture risk assessment. *American Journal of Neuro-*
579 *radiology* 35(10), 1849–1857.
- 580 Yagi, T., Sato, A., Shinke, M., Takahashi, S., Tobe, Y., Takao, H., Murayama,
581 Y., Umezumi, M., 2013. Experimental insights into flow impingement in cere-
582 bral aneurysm by stereoscopic particle image velocimetry: transition from a
583 laminar regime. *Journal of The Royal Society Interface* 10, 20121031.

584 **Figure captions**

585 ***Figure 1.***

586 a) Virtual population of fifty normalised internal carotid artery (ICA) flow wave-
 587 forms. The black wave comprised of fourteen landmarks with errors bars shows
 588 the descriptive statistics of the ICA flow taken from Ford et al. (2005). The red
 589 waves are the GPM-generated ICA flow waveforms. a) Response surface of the
 590 surrogate model of the internal carotid (ICA) mean arterial pressure (MAP).
 591 ICA MAP is 90 mmHg on the red solid line. c) Response surface surrogate
 592 model of the internal carotid (ICA) pressure pulsatility index (PPI). ICA PPI
 593 is 0.5 on the red solid line. d) Intersection of the MAP and the PPI isolines
 594 gives the right terminal resistance (R) and capacitance (C) values for the desired
 595 MAP and PPI at the ICA. e) Reference flow rate waveforms for patients 1 and
 596 2 that are scaled such that the time-averaged wall shear stress (WSS) at the
 597 inlet was 1.5 Pa for each patient. f) CFD-predicted pressure waveforms at the
 598 ICA after choosing the right R and C values.

599 ***Figure 2.***

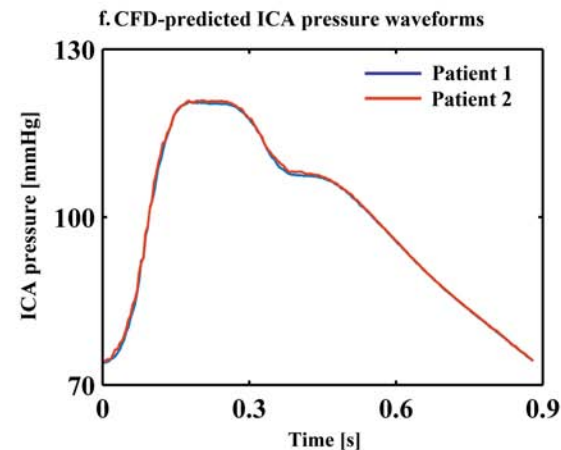
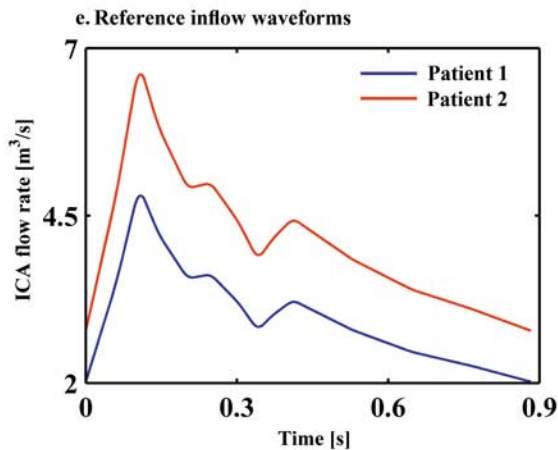
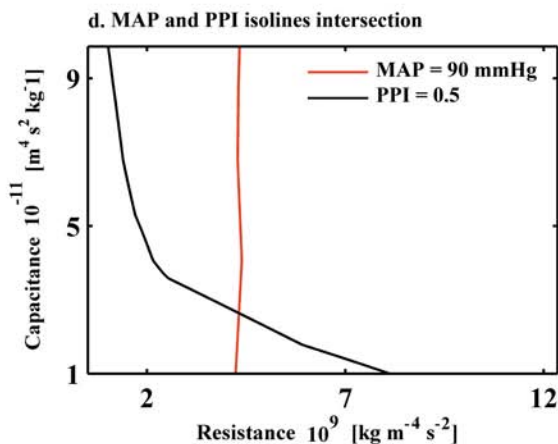
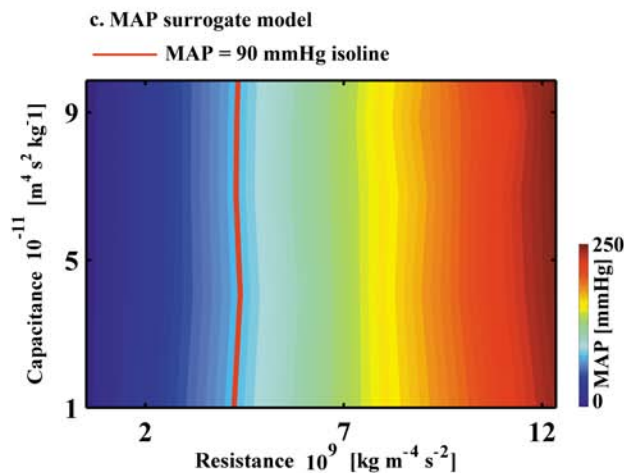
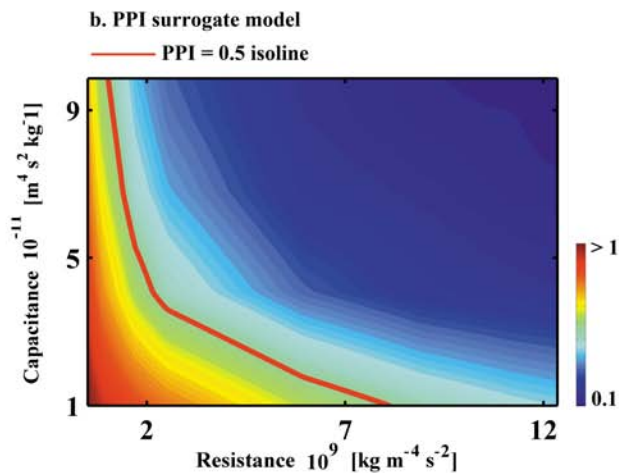
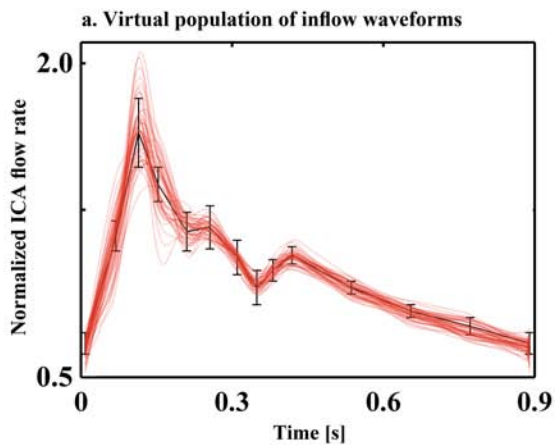
600 The mean values and the coefficients of variation (CoV) of the time-averaged
 601 WSS magnitude (TAWSS), the oscillatory shear index (OSI), and the relative
 602 transverse WSS (rTransWSS) across the virtual population over the aneurysm
 603 walls for patients 1 and 2.

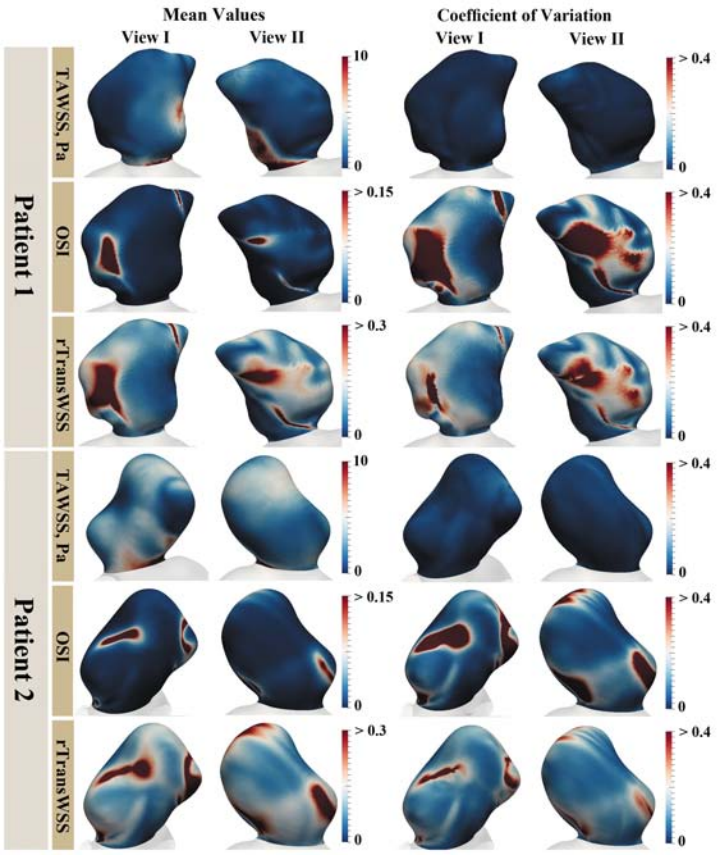
604 ***Figure 3.***

605 The mean values and the coefficients of variation (CoV) of the dominant har-
 606 monic (DH) and axial DH across the virtual population over the aneurysm walls
 607 for patients 1 and 2.

608 ***Figure 4.***

609 Regional variations of the time-averaged WSS magnitude and the relative trans-
 610 verse WSS. Histograms shows the distribution of the coefficient of variations on
 611 each of the atheroprone and atheroprotective regions. A boxplot complementary
 612 illustration is also presented under each histogram.







View I

View II

Mean Values

Coefficient of Variation



View I

View II

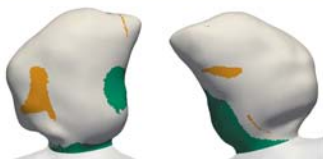
View III

Mean Values

Coefficient of Variation



Patient 1



View I

View II

AtheroprotectiveTAWSS > 3 [Pa]
 $0 < rTransWSS [-] < 0.1$ **Atheroprone** $0 < TAWSS [Pa] < 1$
 $0.3 < rTransWSS [-] < 1$

Patient 2

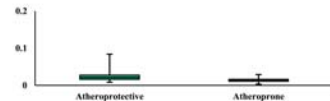
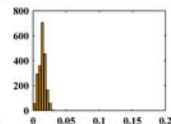
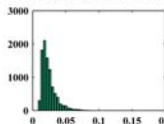
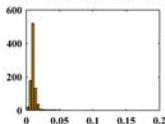
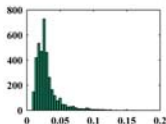


View I

View II

AtheroprotectiveTAWSS > 3 [Pa]
 $0 < rTransWSS [-] < 0.1$ **Atheroprone** $0 < TAWSS [Pa] < 1$
 $0.3 < rTransWSS [-] < 1$

Time-averaged WSS Magnitude (TAWSS) Coefficient of Variation



Relative Transverse WSS (rTransWSS) Coefficient of Variation

